

1 Identifying the seeding signature in cloud particles from hydrometeor  
2 residuals

3 Mahen Konwar<sup>1\*</sup>, Benjamin Werden<sup>2</sup>, Edward C. Fortner<sup>2</sup>, Sudarsan Bera<sup>1</sup>, Mercy Varghese<sup>1</sup>,  
4 Subharthi Chowdhuri<sup>1,&</sup>, Kurt Hibert<sup>3</sup>, Philip Croteau<sup>2</sup>, John Jayne<sup>2</sup>, Manjula Canagaratna<sup>2</sup>, Neelam  
5 Malap<sup>1</sup>, Sandeep Jayakumar<sup>1</sup>, Shivsai A. Dixit<sup>1</sup>, Palani Murugavel<sup>1</sup>, Duncan Axisa<sup>4</sup>, Darrel  
6 Baumgardner<sup>5</sup>, Peter F. DeCarlo<sup>6</sup>, Doug R. Worsnop<sup>2</sup>, and Thara Prabhakaran<sup>1</sup>

7 <sup>1</sup> Indian Institute of Tropical Meteorology, Ministry of Earth Sciences, Pune, India 411008

8 <sup>2</sup>Aerodyne Research Inc., Billerica, MA, USA, 01821

9 <sup>3</sup>Weather Modification Inc., Fargo, ND, USA, 58102

10 <sup>4</sup>Center for Western Weather and Water Extremes, Scripps Institution of Oceanography, La Jolla,  
11 CA 92037, USA

12 <sup>5</sup> Droplet Measurement Technologies, Longmont, CO, USA, 80503

13 <sup>6</sup>Department of Environmental Health and Engineering, Johns Hopkins University, Baltimore, MD  
14 USA 21218

15 <sup>&</sup>now at University of California, Irvine, CA 92697-2700, USA

16

17

18

19

20

21

22 \*Corresponding author

23 Dr. Mahen Konwar

24 Indian Institute of Tropical Meteorology

25 Dr. Homi Bhabha Road, Pune 411 008, India.

26 Email: [mkonwar@tropmet.res.in](mailto:mkonwar@tropmet.res.in)

27

28 **Abstract:**

29 Cloud seeding experiments for modifying clouds and precipitation have been underway for nearly a  
30 century; yet practically all the attempts to link precipitation enhancement or suppression to the  
31 presence of seeding materials within clouds remain elusive. In 2019, the Cloud-Aerosol Interaction  
32 and Precipitation Enhancement Experiment (CAIPEEX) investigated residuals of cloud  
33 hydrometeors in seeded and non-seeded clouds with an airborne mini-Aerosol Mass Spectrometer  
34 (mAMS). The mAMS was utilized in conjunction with a counterflow virtual impactor (CVI) inlet  
35 with a cutoff diameter size of approximately 7  $\mu\text{m}$ . The evaporated cloud droplets from the CVI inlet  
36 as cloud residuals were evaluated through the mAMS. The Chlorine (Cl) associated with  
37 hygroscopic materials, i.e., Calcium Chloride ( $\text{CaCl}_2$ ) and potassium (K), which serve as the  
38 oxidizing agents in the flares, is found in relatively higher concentrations in the seeded clouds  
39 compared to the non-seeded clouds. In convective clouds, Cl and K as cloud residuals were found  
40 even at an distance 2.25 km from the cloud base. Major findings from the seeding impact are: an  
41 increase in the number concentration of small ( $<20 \mu\text{m}$ ) droplets and an indication of raindrop  
42 formation at 2.25 km above the cloud base. It is demonstrated that the seed particle signature can be  
43 traced inside clouds along with the microphysical impacts.

44

45

46

47

48

49

50

51 **1. Introduction:**

52 E.G. Bowen first proposed in 1952 that hygroscopic particles can foster collision-coalescence  
53 (CC) processes in a cloud (Bowen, 1952). Since then, cloud seeding experiments have been  
54 conducted worldwide to mitigate and respond to the ever-increasing urban water demand during a  
55 drought season or in drought-prone regions. More than 50 countries are involved in weather  
56 modification projects (Flossmann, et al., 2019). Over the years, the interest in rain enhancement  
57 projects has increased due to the accumulating evidence of a potentially positive effect (i.e.,  
58 enhancement in rainfall) in several seeding experiments (Mather et al., 1996; Mather et al. 1997;  
59 Bruintjes, 1999; WMO, 2000; Gayatri et al., 2023; Prabhakaran et al., 2023). However, skepticism  
60 remains within the broader cloud physics community because the efficacy of many cloud seeding  
61 experiments remains inconclusive (Ryan and King, 1997; Silverman, 2003; Flossmann et al., 2019).  
62 In addition to the existing challenges of evaluating the effectiveness of cloud seeding experiments,  
63 other pivotal longstanding issues revolve around accurately detecting the hygroscopic particles  
64 released within a cloud, identifying the seeded cloud, and comprehending the impact of seeding on  
65 the cloud microphysical properties.

66 Traditionally, in a cloud seeding experiment tracers such as the inert gas, sulfur hexafluoride  
67 ( $\text{SF}_6$ ) (Rosenfeld et al., 2010; Stith, et al., 1986; Stith et al., 1990; Bruintjes et al., 1995), or radar  
68 chaff at cloud bases are released, and then efforts are made to measure these tracers higher in the  
69 cloud. However, tracing of  $\text{SF}_6$  in a seeded cloud is challenging and successful trials have been  
70 reported only on a few occasions near the cloud base (Rosenfeld et al., 2010). The detection of  $\text{SF}_6$   
71 and chaff traces is hampered by detection limits, especially in the presence of high background  
72 concentrations. Using these tracers as proxies for tracking air masses carrying seeding material is  
73 limited by the challenge of unambiguously connecting their presence with the seeding material due

74 to their non-reactive nature with cloud particles. Consequently, several questions arise during these  
75 experiments. For instance, does the dispersed seeding material effectively enter the targeted cloud  
76 region? Up to what altitude do these materials reach? Are the in-situ measurements being conducted  
77 within the intended cloud volume? How can transported flare particles be located within large  
78 clouds? Due to these uncertainties the need to more quantitatively evaluate the direct link between  
79 seeding materials and the formation of cloud hydrometeors, the development of a low-impact but  
80 more effective tracer has been recommended, e.g. Tessororf et al., (2012).

81 A critical question in any cloud seeding experiment is whether the observed changes in the  
82 cloud microphysical properties after seeding are due to the introduction of seeding material or to  
83 natural cloud processes. There are two requirements necessary to address this question: (i) Can the  
84 trajectory of seeding material be successfully traced in the cloud, and (ii) can changes in cloud  
85 microphysical processing be linked to seeding materials? In this study, an instrumented aircraft was  
86 deployed to acquire convincing evidence that addresses these questions. This work primarily  
87 addresses how to trace seed particles' signatures in clouds and focuses on the question of changes in  
88 cloud microphysical properties due to the introduction of seeding particles. This novel technique  
89 uses a mini-Aerosol Mass Spectrometer (mAMS) (Jayne et al., 2000) behind a counterflow virtual  
90 impactor (CVI) (Noone et al., 1988; Shingler et al., 2012) to identify seeding material in the cloud  
91 droplets residuals i.e., the aerosols that remain after evaporation of the cloud droplets.

92 The hygroscopic cloud seeding hypothesis relies on a chain of microphysical processes.  
93 Dispersal of giant cloud condensation nuclei (CCN), hygroscopic particles with diameter between 1-  
94 10  $\mu\text{m}$ , in the updraft region of cloud base adds larger drops to the tail of the natural cloud droplet  
95 size distribution (DSD), known as the 'tail effect'. This effect further accelerates the formation of  
96 raindrops through CC (Segal et al., 2004; Segal, et al., 2007; Kuba and Murakami, 2010; Konwar et

97 al, 2023). With the initial activation and growth of these larger CCN, the supersaturation over water  
98 droplets ( $SS_w$ ) decreases above the cloud base. As a result, the smaller, natural CCN do not activate.  
99 This effect reduces the total droplet number concentration ( $N_t$ ,  $\text{cm}^{-3}$ ) and broadens the DSDs, a  
100 phenomenon known as the ‘competition effect.’ This broadening fosters the droplet growth rate by  
101 intensifying the CC process, which accelerates the formation of precipitation (Cooper et al., 1997;  
102 Rosenfeld et al., 2010). Past studies used in-situ measurements to evaluate well-formed seeded  
103 clouds whose formation revealed a broadening of the DSDs by hygroscopic seeding in marine  
104 stratocumulus clouds (Ghate et al., 2007). Researchers reported that an increased concentration of  
105 small cloud droplets occurred at an earlier stage, while at a later stage, an increased concentration in  
106 the large size range of 20-40  $\mu\text{m}$  was noted. In another study,  $\text{SF}_6$  was used to track air parcels in a  
107 seeded cloud, where milled salt particles were used as the seeding agent. In this study a broadening of  
108 the DSD was observed (Rosenfeld et al., 2010). Linking the evolution of cloud microphysical  
109 processes to hygroscopic seeding remains elusive despite worldwide hygroscopic cloud seeding  
110 experiments (Flossmann et al., 2019; Silverman 2003; Tessendorf et al., 2012). The major hurdle is  
111 that the physical processes leading to precipitation formation are dynamic and complex and difficult  
112 to directly and quantitatively track and link to the seeding (Tessendorf et al., 2012).

113 In the current study, using an mAMS, we demonstrate that the seeding signatures within  
114 stratus and convective clouds are detectable with an evidence-based approach without using tracer  
115 gasses. We further show that the seeding materials and the seeding-activated cloud droplets in  
116 convective clouds can propagate to higher altitudes while also modulating the cloud’s microphysical  
117 properties. The ultimate goal is to investigate the microphysical pathways that are modified in cloud  
118 seeding operations. These experiments took place in the region near Solapur ( $17.66^\circ$  N,  $75.90^\circ$  E),

119 India, during the Cloud-Aerosol Interaction and Precipitation Enhancement Experiment (CAIPEEX)  
120 (Prabha et al., 2011; Kulkarni et al., 2012; Prabhakaran et al., 2023) in 2019 (phase-IV).

## 121 **2. Materials and Methods:**

### 122 **2.1 Measurements of cloud properties.**

123 Three cloud seeding events carried out on 21 August, 23 August and 24 August in 2019, are  
124 selected here for evaluation of seeding signatures and plausible links to microphysical properties.  
125 Instruments for the measurement of flare particles, aerosol, and cloud properties were operated on a  
126 Beechcraft-B200 aircraft. This aircraft was equipped with flare racks located under both the wings  
127 and the belly. The flare racks in the wings are used for warm cloud seeding operations (Mather et al.,  
128 1997), while the belly is utilized for cold cloud seeding operations (French et al., 2018; Friedrich et  
129 al., 2020). The temperature ( $T$ , °C), relative humidity (RH%), wind speed ( $\text{ms}^{-1}$ ) and wind directions  
130 were measured with the Airborne Integrated Meteorological Measurement System (AIMMS-20).  
131 The DSD in the size range of 2-50  $\mu\text{m}$  was measured with a Cloud Droplet Probe (CDP-2)  
132 manufactured by Droplet Measurement Technologies LLC, USA. The bulk microphysical properties  
133 are derived from the measured DSDs, e.g. the total number concentration ( $N_t$ ,  $\text{cm}^{-3}$ ) and liquid water  
134 content (LWC,  $\text{g m}^{-3}$ ). The effective radius ( $r_e$ ,  $\mu\text{m}$ ) was calculated from the ratio between the third  
135 and second moments of the DSDs (Martin et al., 1994). The Precipitation Imaging Probe (PIP) was  
136 used to document drizzle drops in the cloudcover the size range of 100-6200  $\mu\text{m}$ . The technical  
137 specifications of these instruments are shown in Table 1. The uncertainties associated with the CDP,  
138 and single particle light scattering instruments like the CDP, have been well characterized and  
139 documented (Baumgardner et al., 1983, 2001, 2016; Lance et al., 2010). In water droplets the sizing

140 uncertainty is  $\pm 20\%$  and counting accuracy  $\pm 16\%$ , which propagates into a LWC uncertainty of  
141  $\pm 38\%$ .

142 Cloud properties are altered by the entrainment of cloud-free air masses at the edges of the  
143 cloud; hence to minimize the influences of entrainment and mixing processes in the seeded and non-  
144 seeded clouds, only clouds with near adiabatic or slightly diluted cloud parcels are considered to  
145 evaluate cloud microphysical properties. Only cloud passes with LWC in the range of  $0.75 <$   
146  $LWC/LWC_{\max} < 1$  (Konwar et al., 2021) were selected for this study. Here,  $LWC_{\max}$  represents the  
147 maximum measured value of LWC during a cloud pass. Note that this cloud regime may be  
148 considered as the cloud core, typically located within the strongest updrafts zone. Our main aim is to  
149 select the DSDs located within the cloud core regime. Note that in most naturally developing clouds  
150 the  $LWC_{\max}$  values are less than the adiabatic LWC ( $LWC_{\text{ad}}$ ) values because of the entrainment of  
151 drier air, mixing, precipitation fallout and radiative heating/cooling (Korolev et al., 2007). The  
152 maximum adiabatic fraction,  $AF_{\text{mx}}=LWC_{\max}/LWC_{\text{ad}}$ , indicates the extent of dilution that has  
153 occurred in the cloud core regime. During their development and dissipation stages clouds undergo  
154 significant changes; therefore, it is practically impossible to find two clouds identical in all states, let  
155 alone their lifetimes. It is to be noted that the AF values may not accurately represent the mixing  
156 state when CC is significant and drizzle particles form within the clouds. Additionally, studies of the  
157 seeding effect using parcel model simulations without the inclusion of mixing processes indicates a  
158 significant change in the LWC profile compared to the non-seeded cloud (Konwar et al., 2023). Such  
159 changes in LWC values at different vertical distances from the cloud base of the seeded clouds do  
160 not necessarily imply the true dilution rate in the observations. At a given height, however, seeding  
161 does not change the adiabatic value, but activation of new particles at a given level due to seeding  
162 can alter the AF. Another aspect is that near the cloud base the  $LWC_{\text{ad}}$  values are quite small (e.g.,  $<$

163  $1 \text{ g m}^{-3}$ ), therefore any small change in the measured LWC could indicate a large change in AF. With  
164 this background information in mind, the DSDs for Seed Cloud (SCI) and No Seed Cloud (NSCI)  
165 conditions are compared at different vertical distances above the cloud base ( $D^*$ , km). The lowest  
166 unbroken visible section of a convective cloud was selected as the cloud base. The cloud top is  
167 defined as the maximum altitude attained by these clouds at any given moment during their  
168 development.

169



170

171

**Table 1**

172

Details of Instruments used on the aircraft and for offline analysis in the study

Instrument	Variable	Range/Remark	Reference
Aventech AIMMS-20	GPS Coordinates, altitude above Mean Sea Level (MSL), temperature, dew point temperature, horizontal and vertical winds	Vertical wind accuracy 0.75 m s <sup>-1</sup>	<a href="https://aventech.com/products/aimms20.html">https://aventech.com/products/aimms20.html</a>
DMT CDP2	Cloud droplet number concentration and size distribution	3.0 – 50.0 μm	<a href="https://www.dropletmeasurement.com/product/cloud-droplet-probe/">https://www.dropletmeasurement.com/product/cloud-droplet-probe/</a>
DMT PIP	Particle image	100 μm – 6.2 mm	<a href="https://www.dropletmeasurement.com/product/precipitation-imaging-probe/">https://www.dropletmeasurement.com/product/precipitation-imaging-probe/</a>
CVI	Droplet/ice crystal residuals	Particle Cut size ~ 7μm	<a href="https://www.brechtel.com/product/aircraft-based-counterflow-virtual-impactor-inlet-system-cvi/">https://www.brechtel.com/product/aircraft-based-counterflow-virtual-impactor-inlet-system-cvi/</a>

173

174

175

176

177 **2.2 Measurement of hygroscopic flare particles by mAMS and Correcting time trends of slow-**  
178 **vaporizing species**

179 We utilized a mAMS to analyze the chemical compositions of residual particles from cloud droplets,  
180 specifically to trace flare particles within the seed clouds. The CVI is manufactured by Brechtel  
181 Manufacturing Inc. (BMI, Model 1204, [www.brechtel.com](http://www.brechtel.com)). The cloud droplets were passed through  
182 the CVI to obtain the droplet residual that were sampled by the mAMS. Through the use of inertial  
183 impaction, the CVI inlet allows cloud hydrometeors with aerodynamic diameters larger than a  
184 certain size to pass through, depending on the velocity of the counterflow. A warm, particle-free dry  
185 nitrogen gas is directed towards the inlet against the direction of the ambient air flow. This causes a  
186 separation of in the incoming free stream air, with particles  $>7 \mu\text{m}$  in the sampled air having enough  
187 inertia to penetrate the counterflow and join the sample flow. The CVI adjusted flow rates with its  
188 internal software based on true air speed (TAS) obtained from the AIMMS. The cut-size is a  
189 function of various factors, e.g., air pressure, air speed, and the average angle of attack, is known to  
190 have an uncertainty of approximately  $\pm 1 \mu\text{m}$ . The heated air evaporates cloud droplets and the  
191 remaining dried residuals enter the mAMS where their chemical compositions are classified. Details  
192 of the operational principles of the CVI can be found in Ogren et al., 1985; Ogren, 1987; Noone et  
193 al., 1988; Shingler et al., 2012; Golderger et al. 2020; and references therein.

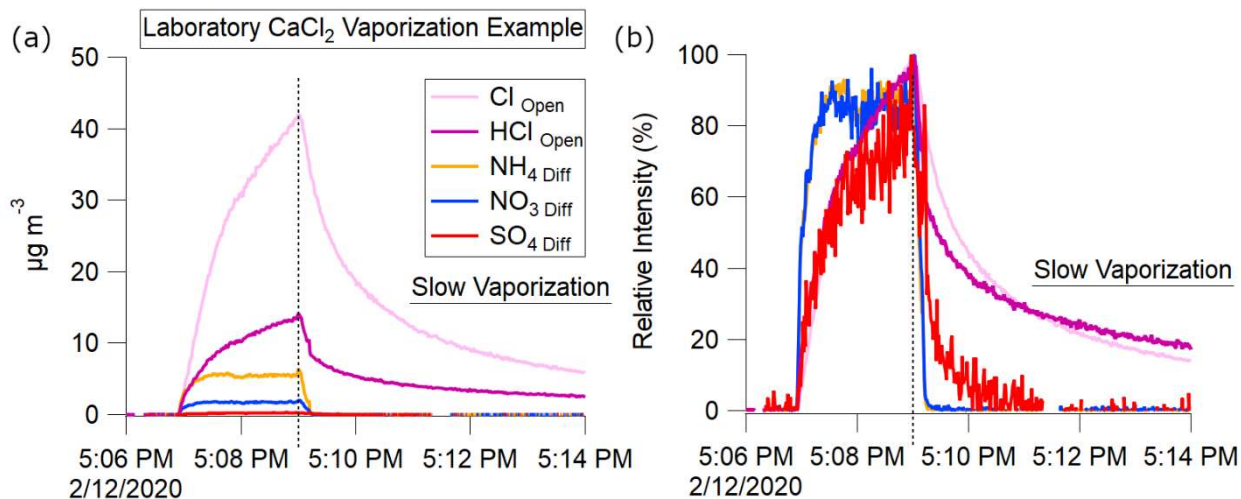
194 The mAMS measured the residual particles with vacuum aerodynamic diameters of less than  $1 \mu\text{m}$ ,  
195 sampling through an aerodynamic lens. The aerosol sample stream is intermittently blocked to  
196 measure background signals. The aerosol signal is the difference between unblocked ("open")  
197 measurements and those obtained during the blocked ("closed") period. The mAMS sampled 10  
198 seconds of closed signal for every 110 seconds of open. The heater, operated at  $600 \text{ }^\circ\text{C}$ , vaporized  
199 the sample, electron impact ionized the vapors, and the resultant ions were extracted into the mass

200 analyzer for measurement of chemical composition and mass distributions (Jayne et al., 2000;  
201 DeCarlo et al., 2006; Canagaratna, et al, 2007; Drewnick et al., 2015; Giordano et al., 2018; Salcedo  
202 et al., 2006).

203 Ice Crystal Engineering (ICE) Inc. (USA) manufactured the hygroscopic flares used in this  
204 work. The flares were composed of an aggregated mixture of potassium perchlorate ( $\text{KClO}_4$ ) and  
205 calcium chloride ( $\text{CaCl}_2$ ) (Hindman, 1978; Bruintjes et al., 2012).

206 For non-refractory ambient aerosol species (i.e.,  $\text{NH}_4$ ,  $\text{NO}_3$ ,  $\text{SO}_4$ ) aerosol concentrations are  
207 obtained from the difference between the open and closed signals. The vaporization of non-  
208 refractory aerosol species at  $600^\circ\text{C}$  typically completes on the timescale of hundreds of  
209 microseconds, however, semi-refractory species such as metals and salts may take minutes to  
210 completely vaporize (Canagaratna et al., 2007; Salcedo et al., 2006).

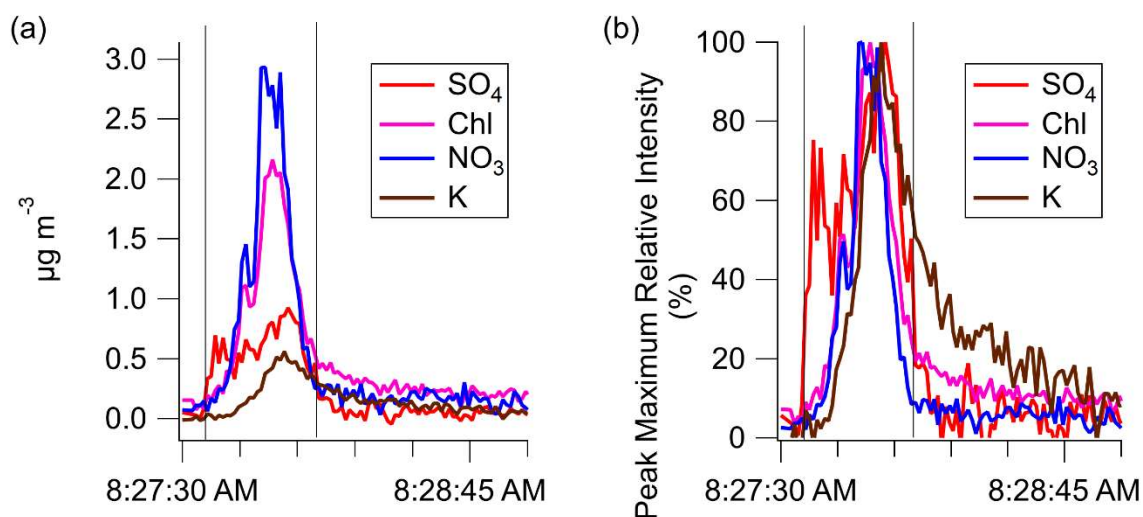
211 As discussed below, the Cl, HCl, and K from the  $\text{KClO}_4$  and  $\text{CaCl}_2$  in flares is a semi-  
212 refractory species which exhibits slow vaporization. These slow vaporizing species were analyzed  
213 using only the open signals. The background signal was calculated from measurements obtained  
214 immediately before the cloud intercept of interest.



215  
 216 **Figure 1.** Laboratory atomized CaCl<sub>2</sub> AMS measurements observing slow vaporization of semi-  
 217 refractory Cl species on 2/12/2020. Atomization begins at 5:07 PM ending at 5:09 PM. Slow  
 218 vaporization is evident after 5:10 PM. The presence of NO<sub>3</sub>, NH<sub>4</sub>, and SO<sub>4</sub> are from calibration  
 219 species (NH<sub>4</sub>NO<sub>3</sub>, NH<sub>4</sub>SO<sub>4</sub>) contaminants in the atomizer.

220 CaCl<sub>2</sub>, the seeding component in the flares, has a melting point of 774 °C. Laboratory  
 221 measurements of atomized CaCl<sub>2</sub>, primarily detected as Cl and HCl ions, exhibit the same slow  
 222 vaporization seen in refractory salts (Drewnick et al., 2015). Fig. 1 shows a comparison of  
 223 vaporization timescales of CaCl<sub>2</sub>, NH<sub>4</sub>NO<sub>3</sub>, and (NH<sub>4</sub>)<sub>2</sub>SO<sub>4</sub> obtained with an AMS during laboratory  
 224 measurements of CaCl<sub>2</sub> in solution with H<sub>2</sub>O which had been atomized and passed through a drier  
 225 before sampling. This behavior differs from that observed from non-refractory NH<sub>4</sub>NO<sub>3</sub> and  
 226 (NH<sub>4</sub>)<sub>2</sub>SO<sub>4</sub>, which were present as tracers.

227



228  
 229 **Figure 2.** (a) shows the slowed time response of the species K and Cl for a seeded cloud pass on  
 230 August 23<sup>rd</sup> (b) the relative intensity with respect to peak maximum of each species highlights the  
 231 slowed decay of K and Chl compared to  $\text{SO}_4$  or  $\text{NO}_3$ .

232 The seeded cloud pass shown in Fig. 2a illustrates a single seeded cloud pass. The K and Cl  
 233 time series have a delayed decay to background compared to sulfate or nitrate. The relative intensity  
 234 shown in Fig. 2b highlights the delayed response in the decay of the two flare associated species (K,  
 235 Cl).

236 An exponential decay was fit to each cloud intercept, from the signal peak to 5 e-folding  
 237 times. The average decay exponential ( $\tau$ ) for Cl, and K across all seeded cloud intercepts, is shown in  
 238 Table 2.

239  
 240  
 241

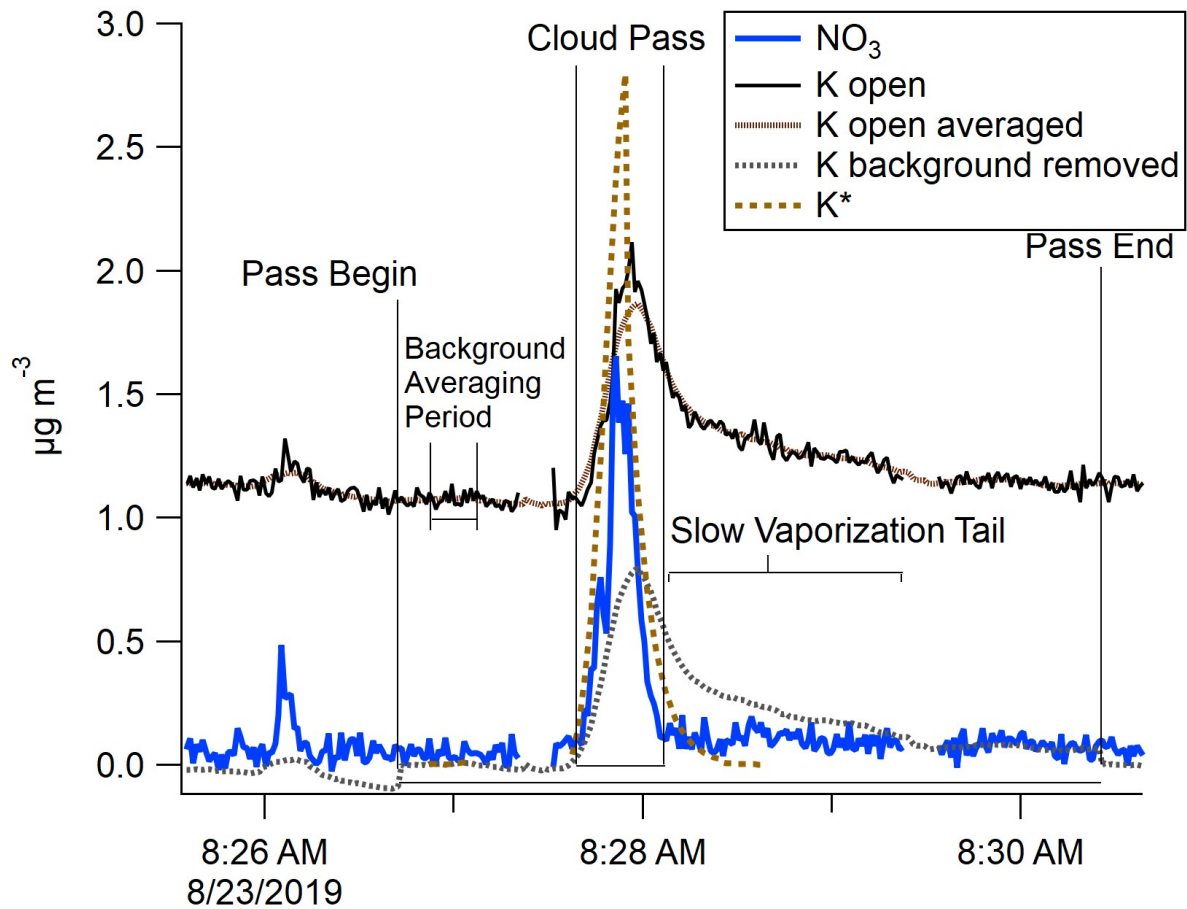
242

**Table 2**

243 Average decay time constants from seeded cloud intercepts during CAIPEEX- IV, 23 August 2019.

T	K	HCl	Cl
Mean	6.7	3.4	3.3
Std Dev	2.3	0.5	0.8

244



245

246 **Figure 3.** The measured semi-refractory open K signal and corrected K\* signal from the mAMS are  
 247 depicted for a seeded cloud pass on 23 August 2019. The periods from the beginning to the end of  
 248 the cloud passes are also shown.

249

250 For each slowly vaporizing species, a new corrected time series was created. The start, stop, and  
 251 maximum total mass times were identified for each cloud pass (Fig. 3). For each species, a  
 252 background signal was determined from measurements during the non-cloud period preceding each  
 253 pass. This background was subtracted from the signal observed during each cloud intercept.

254 The cloud intercept time series peak at the same time as the uncorrected series. However, the tails  
 255 were corrected to decay within 5 tau e-folding times, while preserving the total mass. The equations  
 256 used in these calculations are shown below.

257 The measured mass from the start of the pass to the end of the slow vaporization regime was scaled  
 258 by the ratio of the total area divided by the area of fast vaporization (equation 1)

$$259 \text{Conc.}_{AreaCorrected}(t) \Big|_{End+(5\tau)}^{Start} = (\text{Conc.}(t) - \text{Conc.}_{Background}) * \frac{Area_{Peak+Tail}}{Area_{Peak}} \quad (1)$$

260 The decay of this normalized mass is adjusted to the exponential decay fit (Table 2) to the slow  
 261 vaporized mass (equation 2). This decay extends from the cloud pass peak to the end of the normal  
 262 vaporization period plus five e-folding times (Giordano et al., 2018)

$$263 \text{Conc.}_{TailCorrected}(t) \Big|_{End+(5\tau)}^{Peak} = \text{Conc.}_{AreaCorrected}(t) * e^{-(\frac{1}{\tau})t} \quad (2)$$

264 This decay-corrected time-shifted time series is normalized to the unmodified slow vaporizing total  
 265 mass (equation 3)

$$266 \text{Conc.}_{Corrected}(t) \Big|_{End}^{Start} = \text{Conc.}_{TailCorrected}(t) * \frac{Area_{Peak}}{Area_{Peak} + Area_{Peak+Tail}} \quad (3)$$

267

268 Finally, we applied an enhancement factor correction to the mAMS data resulting from the ambient  
 269 aerosol concentration being concentrated in the CVI by following Shingler et al., (2012).

## 270 **3. RESULTS**

### 271 **3.1.1 Slow vaporization of semi-refractory seed aerosols**

272 Although many aerosol species readily vaporize at 600 °C, some semi-refractory materials in nature  
273 do not. Submicron aerosol particles in the troposphere, that contain Cl, are rarely semi-refractory  
274 and vaporize quickly in the mAMS. However, Cl in seeded clouds was found to vaporize slowly.  
275 The Cl measured in clouds seeded using CaCl<sub>2</sub> and KClO<sub>4</sub> exhibited the same slow vaporization  
276 (Fig. 2) as Atomized CaCl<sub>2</sub> in the laboratory (Fig 1). The majority of atmospheric Cl-containing  
277 aerosols are non-refractory. In our study the slowly vaporizing Cl was only observed in seeded  
278 clouds; thus, we assume that the source of the slow vaporizing Cl was from the flare material.  
279 Aerosol K is uncommon except as super micron mineral dust. As shown in Fig.2b, slowly vaporizing  
280 signals of Cl and K were observed in the campaign during seeded cloud intercepts.

281 The combination of the isolation of cloud residuals by the CVI and the presence of K and semi-  
282 refractory Cl allow for discrimination of the particles containing the flare combustion products.

283 The element Ca, was also present in the flare. The boiling point of Ca of 1484 °C at ambient  
284 pressure means that this species was not vaporized inside the AMS and is thus considered a  
285 refractory species. Since Ca could not be observed in our study, the focus remained on the other  
286 species present.

287 As previously discussed, the time series of semi-refractory Cl and K signals are corrected to account  
288 for the difference in the decay response of slowly vaporizing species in the mAMS. Fig. 3 depicts  
289 the corrected (K\*) and uncorrected semi-refractory K signals in the mAMS measurements for a  
290 seeded cloud pass, defining the periods for the start, peak, end, and tail of the pass.

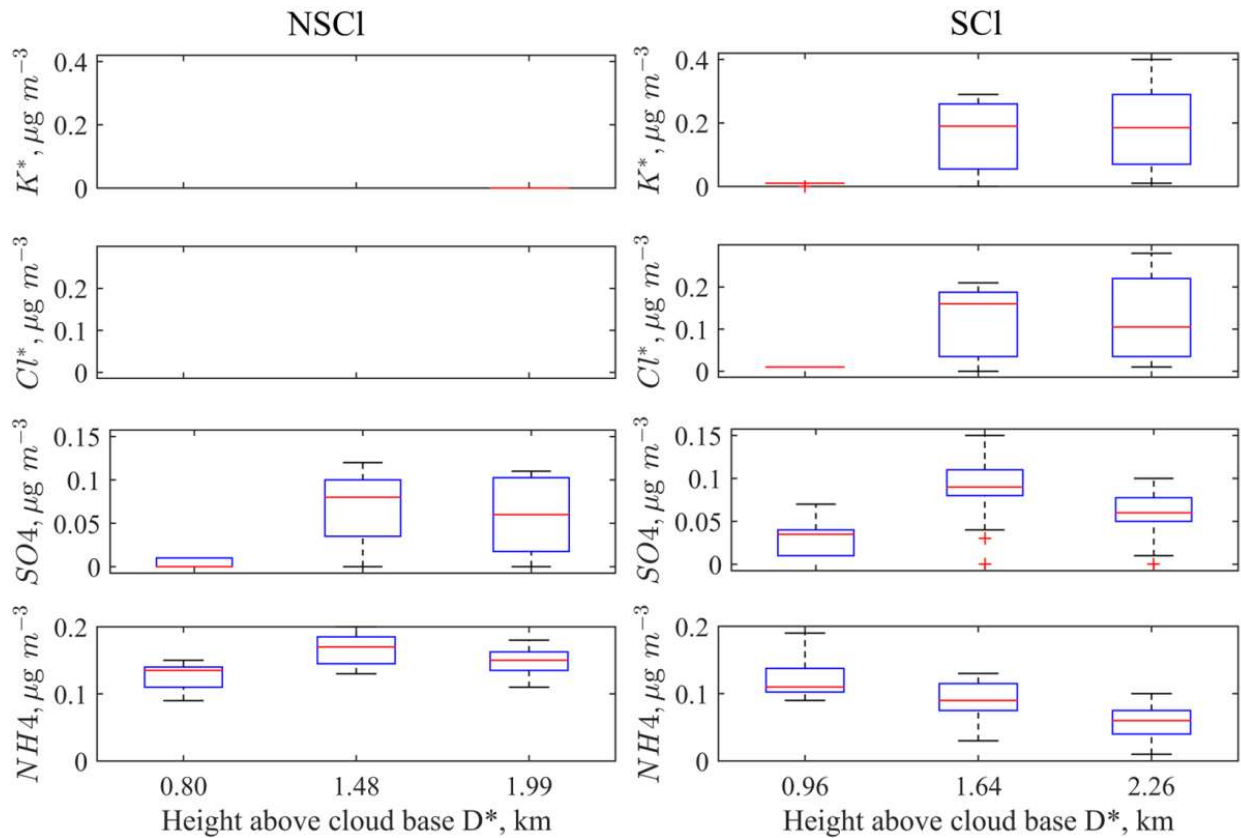
291



292

293

294



295

296 **Figure 4.** mAMS measurements of the mass concentrations of  $Cl^*$ ,  $K^*$ ,  $NO_3$ , and  $SO_4$  versus  $D^*$

297 (km) for cloud particle residuals from six cloud passes through the same cloud on 23 August 2019.

298 The vertical profile box plots of each mAMS species at different altitudes shows median

299 concentration and range (25-75<sup>th</sup> percentiles). Three non-seeded clouds (NSCI) and three seeded

300 clouds (SCI) are shown.

301

302 A vertical profile of cloud residual aerosols, within the same cloud, taken before and after  
303 seeding, provides a platform for measuring and observing cloud physical and chemical changes. The  
304 resultant mAMS measurements from one such experiment, on August 23, 2019, with three cloud  
305 passes of the same cloud before and three passes after seeding are shown in Fig 4.

306 In the mid level, all chemical species were found in higher quantities in the seeded cloud than in the  
307 non-seeded cloud. Cl and K concentrations were significantly increased for all seeded cloud passes  
308 compared to non-seeded cloud passes. The measurement of the flare chemical species in the seeded  
309 cloud indicates that the mAMS could successfully identify the cloud droplets that containing  
310 seeding material.

311 An additional observation is the increased  $\text{NO}_3$  and  $\text{SO}_4$  concentration in the cloud drops of seeded  
312 clouds at upper heights. We hypothesized that the increased concentrations of these two chemical  
313 species could be linked with the activation of the flare particles and other organics while mixing with  
314 the naturally available  $\text{NO}_3$  and  $\text{SO}_4$  aerosols. The increased concentration of  $\text{NO}_3$  in the seeded  
315 cloud may also be due to the presence of more LWC. The additional water drives nitric acid ( $\text{HNO}_3$ )  
316 from gas to liquid  $\text{NO}_3$  (Wang and Laskin, 2014).

317 This example highlights the ability of the mAMS to identify flare associated species, by both  
318 increased concentration and time response, in order to confirm the presence of seeding material in  
319 cloud droplet residual.

320

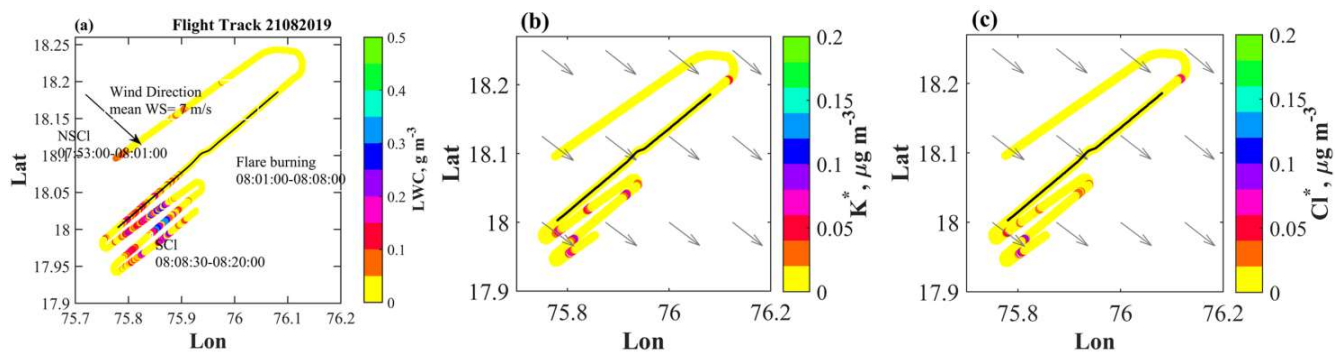
## 321 **3.2 Seeding experiment, Seeding Signature, and Cloud properties**

322 **3.2.1. Case i: 21 August 2019.** The flight pattern of the aircraft during the cloud seeding  
323 experiment conducted on 21 August 2019 in a warm stratus layer is shown in Fig. 5a. The objective

324 was to identify the seeding materials and record the cloud microphysical properties. The wind  
325 direction was north-westerly at an altitude of nearly 4.10 km with a mean wind speed of  $7 \text{ ms}^{-1}$ .  
326 Cloud passes ( $T=5.14 \text{ }^\circ\text{C}$ ,  $H=4.39 \text{ km}$ ) were made through the stratus layer before the dispersal of  
327 seeding materials. Four hygroscopic flares were burned, two at a time, inside the layer cloud, from  
328 8:01-8:08 UTC at  $H=4.10 \text{ km}$ . Weak updrafts ( $W=0.61\pm 1.53 \text{ m s}^{-1}$ ) prevailed indicate that the flare  
329 material might have drifted horizontally. Increased mass concentrations of  $\text{K}^*$  and  $\text{Cl}^*$  are noted in  
330 the downwind after the dispersal of the seeding agents, as shown in Fig. 5b and 5c. Repeated  
331 crosswind cloud passes at a similar level ( $T= 6.44 \text{ }^\circ\text{C}$ ,  $H= 4.10 \text{ km}$ ) were made downwind of the  
332 seeding. The aircraft could release non-volatile and fine aerosol particles through exhaust emission  
333 (Anderson et al., 1998), which may also contaminate the cloud mass. Prabhakaran et al. (2023)  
334 measured aerosol size distribution of background air mass, and then the background with aircraft  
335 exhaust during CAIPEEX. They reported that the aircraft exhaust can impact mean radius, spectral  
336 width and number concentrations of different modes of log-normal aerosol size distribution (see the  
337 supplementary materials at <https://doi.org/10.1175/BAMS-D-21-0291.2>). Solution of simple  
338 advection equations indicates dispersal of seeding plumes in the downwind region after nearly 3  
339 minutes (not shown here) where the aircraft also recorded enhanced concentrations of  $\text{K}^*$  and  $\text{Cl}^*$ .  
340 Gayatri et al., (2023) illustrated the seeding impact downwind of the seeded area through the high-  
341 resolution numerical model in similar monsoon environment with the monsoon low-level jet (LLJ)  
342 as detailed in the present study. The cloud bases are situated very close to the region with high wind  
343 speeds in the monsoon low-level jet and the advection of seeding plume downwind of the seeded  
344 location is noted. However, the fact that seeding was done specifically in the strong updraft zones  
345 and the seed particles were also lifted inside the cloud and more cloud droplets were noted both in  
346 the observations and simulations. Earlier, during the Seeded and Natural Orographic Wintertime

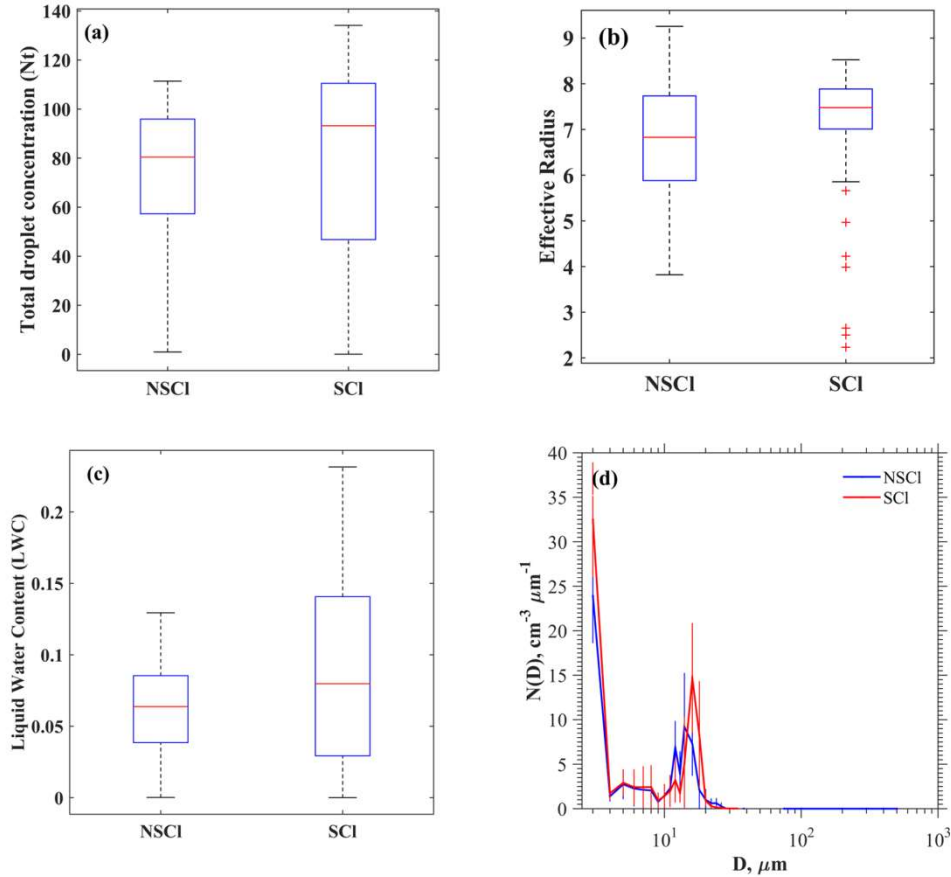
347 Clouds: The Idaho Experiment (SNOWIE) (Xue et al., 2022) noted seeding plumes dispersed within  
348 orographic clouds in more than 1 hour along the slanted downwind direction.

349



350

351 **Figure 5.** (a) The flight path during the seeding experiment on 21 August 2019 color coded by LWC  
352 at 1 Hz resolution. Periods during which cloud measurements were made for non-seeded clouds  
353 (NSCI) and seeded clouds (SCI) are annotated. Mass concentrations of (b)  $K^*$  and (c)  $Cl^*$  during the  
354 seeding experiment are shown along the flight track. The ambient wind fields shown as arrow  
355 obtained from <https://cds.climate.copernicus.eu/> ( $0.25^\circ \times 0.25^\circ$ ), which are resampled to  $0.125^\circ \times$   
356  $0.125^\circ$ . A small area of elevated  $K$  and  $Cl$ , prior to the flare burning is noted. This was measured  
357 outside the cloudy region as suggested by the LWC values and it might be appeared probably due to  
358 other unknown sources.



359

360 **Figure 6:** Box plots of (a) total droplet concentrations, (b) Effective radius, (c) LWC are shown for  
 361 NSCI and SCI. (d) Mean cloud DSDs with standard deviations (vertical bars) are depicted indicating  
 362 the variability. The selected DSDs fall within the criteria of  $0.75 < \text{LWC}/\text{LWC}_{\text{max}} < 1$ .

363 Stratus cloud passes were selected for study based on two criteria: a cloud pass duration  
 364 greater or equal to 5 seconds and  $N_t > 10 \text{ cm}^{-3}$ . Two NSCI cloud passes made during 7:53:00-7:53:31  
 365 UTC and 7:55:17-7:55:41 UTC were chosen for the analysis. After the flares had dispersed, three  
 366 passes during 08:08:37-08:08:45 UTC, 8:09:42-8:09:53 UTC, and 8:09:59-08:10:39 UTC were  
 367 selected based on the elevated levels of detection of K and Cl ( see Fig. 5b and 5c). Box plots of  $N_t$ ,  
 368  $r_e$  and LWC are displayed for NSCI and SCI in Figs. 6a, b and c, respectively. It is worth noting that  
 369 the SCI cases exhibit greater median values for these three parameters. The properties of DSDs along

370 the cloud pass are shown in Supplementary Figs. S1 and S2. The DSD properties and mass  
371 concentrations of  $K^*$  and  $Cl^*$  are provided in Table 3. Increased droplet concentrations in the  
372 smallest size bin are noted after a few minutes from the seeding time while drizzle drops were not  
373 observed in the SCl. Comparisons are made for mean SCl-DSD and NSCl-DSD in the range  
374  $0.75 < LWC/LWC_{max} < 1$ , as illustrated in Fig. 6d. An increase of  $N(D)$  at  $D \approx 3 \mu m$  and in the size  
375 range  $13 < D < 20 \mu m$  are noted in the SCl, while  $N(D)$  decreased in the size range  $4 < D < 13 \mu m$ .  
376 The increase in the smallest cloud droplets may be due to freshly nucleated aerosols, likely due to  
377 the activation of seeding materials. The increase in the mid-size droplet concentrations could be due  
378 to the activation of coarse mode aerosols and subsequent diffusional growth. Since drizzle drops  
379 were not formed, it may suggest that hygroscopic seeding in stratus cloud with low LWC value e.g.  
380  $< 0.5 g m^{-3}$  may not yield a significant positive seeding effect for the production of drizzle.

381

### 382 **3.2.2 Case ii: 23 August 2019.**

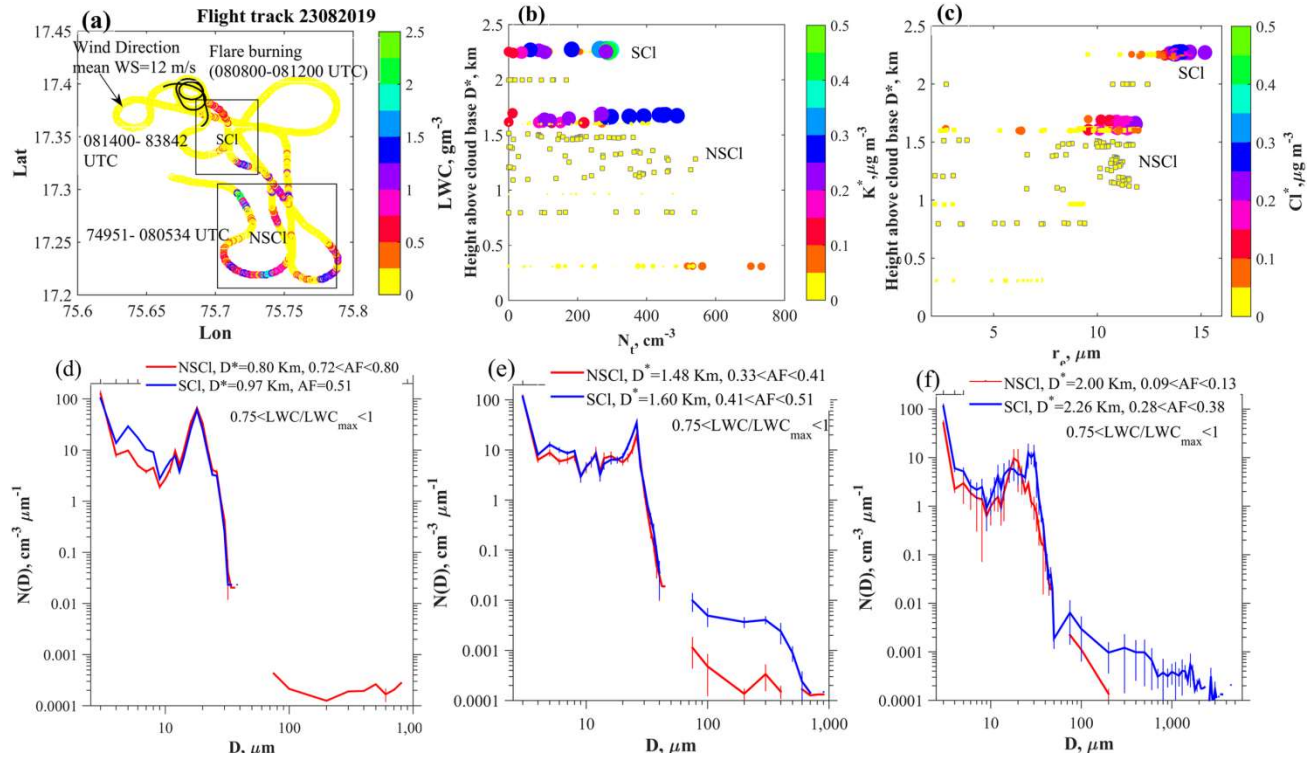
383 Fig. 7a depicts the flight patterns for the case on 23 August 2019. This seeding event is selected for  
384 evaluation because (i) The SCl and NSCl convective clouds were isolated and in the growing and  
385 non-precipitating stages, (ii) the cloud top was below freezing level (5 km) therefore ideal for  
386 studying warm rain microphysics, (iii) The SCl and NSCl were formed within the same area (20 km  
387 x 20 km) and lastly, (iv) both the SCl and NSCl grew to similar cloud top altitudes ( $\approx 4$  km),  
388 therefore roughly at similar growth stages. These conditions made this case suitable for evaluating  
389 the seeding effect on warm rain. The cloud base height over the observational area was nearly 1.80  
390 km. Northwesterly winds (mean wind speed of  $12 ms^{-1}$ ) prevailed in the boundary layer at 1.30 km  
391 (850 mb). Before the dispersal of flare materials at cloud base, the cloud microphysical properties of  
392 NSCl were measured from 7:49 to 8:06 UTC by step-wise multiple cloud penetrations from the top

393 ( $\approx 3.90$  km) to near the cloud base ( $\approx 1.80$  km). A maximum updraft of  $4.40 \text{ ms}^{-1}$  was observed at  
394 the cloud base. After completion of NSCI measurements, the aircraft then circled below the cloud  
395 base and burned four hygroscopic flares (two on each wing) in the updrafts during 8:08-8:12 UTC,  
396 followed by several step-wise cloud penetrations at nearly 1000 ft intervals, from near the cloud base  
397 to cloud-top during the period 8:14-8:28 UTC.

398 The profiles of  $N_t$  and  $r_e$  *w.r.t.* the  $D^*$ s are shown in Fig. 7(b,c). The mass concentrations of  
399  $K^*$  and  $Cl^*$  corresponding to  $N_t$  and  $r_e$ , respectively, are also indicated. The statistical properties of  
400 the DSD parameters are presented in Table 3. The variations of DSDs along the cloud transects,  
401 values of  $r_e$ , drizzle concentration, LWC, and  $W$  are shown in the supplementary material's Figs. S3-  
402 4. Note that the SCI and NSCI were not identical due to the natural variability discussed previously,  
403 with this background the following observations are noted:

404

405



406  
407

408 **Figure 7.** (a) Flight track during the seeding experiment on 23 August 2019. The flight track during  
 409 the flare burning period is overlaid with black color. The areas of seeded cloud (SCI) and non-seeded  
 410 cloud (NSCI) are indicated on the figure panels. The arrow indicates the wind direction near the  
 411 cloud base height of 1.80 km. The color bar indicates the liquid water content (LWC,  $\text{gm}^{-3}$ ) of  
 412 clouds. Profiles of (b)  $N_t$ , ( $\text{cm}^{-3}$ ) and (c)  $r_e$ , ( $\mu\text{m}$ ) *w.r.t.* height above cloud base,  $D^*$  (km) are shown.  
 413 The parameters are indicated in the color bars with the mass densities of  $K^*$  and  $Cl^*$ , ( $\mu\text{g m}^{-3}$ ). The  
 414 squares with black edges indicate NSCI, while filled circles indicate SCI. The sizes of the symbols  
 415 increase with increasing mass of the chemical components. Mean cloud drop size distributions with  
 416 standard deviations indicated by the error bars of slightly diluted clouds ( $0.75 < \text{LWC}/\text{LWC}_{\text{max}} < 1$ ) at  
 417 various  $D^*$  (km), for NSCI and SCI, (d), (e) and (f).

418



420 Cloud properties of Non-Seeded Cloud (NSCI) and Seeded Cloud (SCI) along the cloud transect are  
 421 shown. Vertical distance above the cloud base ( $D^*$ , km), Mean values and standard deviation of total  
 422 droplet concentration  $N_t$ , ( $\text{cm}^{-3}$ ) in the diameter range 2-50  $\mu\text{m}$ , maximum droplet concentration  
 423 ( $N_{t\text{max}}$ ,  $\text{cm}^{-3}$ ), mean effective radius ( $r_e$ ,  $\mu\text{m}$ ), liquid water content (LWC,  $\text{gm}^{-3}$ ), Maximum LWC  
 424 ( $\text{LWC}_{\text{max}}$ ), maximum adiabatic fraction ( $\text{AF}_{\text{mx}} = \text{LWC}_{\text{max}}/\text{LWC}_{\text{ad}}$ ), where  $\text{LWC}_{\text{ad}}$  is the adiabatic  
 425 LWC calculated from a parcel model.  $\text{AF}_{\text{mx}}$  for layer clouds on 21082019 is not calculated. The  
 426 mean of small droplet concentration ( $D < 11 \mu\text{m}$ ) and the maximum of small droplet concentration,  
 427 and drizzle concentration (DrizzleCon, ( $\text{cm}^{-3}$ ) are also shown. Concentrations of  $\text{K}^*$  and  $\text{Cl}^*$  in  $\mu\text{g m}^{-3}$   
 428  $^3$  during NSCI and SCI observations are indicated. Due to limited field calibrations, the  
 429 concentrations presented here are nitrate equivalent. Below Detection Limit (BDL) data are  
 430 indicated.

Case	$D^*$ (km)	$N_{\text{tmn}}$ $\pm\text{SD}$ ( $\text{cm}^{-3}$ )	$N_{\text{tmax}}$ ( $\text{cm}^{-3}$ )	$r_e$ $\pm\text{SD}$ ( $\mu\text{m}$ )	LWC $\pm\text{SD}$ ( $\text{gm}^{-3}$ )	LWC <sub>max</sub> ( $\text{gm}^{-3}$ )	$\text{AF}_{\text{mx}}$	$N_{\text{tmn}}, [N_{\text{tmx}}]$ ( $D < 11 \mu\text{m}$ )	DrizCon $\pm\text{SD}$ ( $\text{cm}^{-3}$ )	Mean $\text{K}^*$ $\pm\text{SD}$ [ $\text{K}^*_{\text{Max}}$ ] $\text{mg m}^{-3}$	Mean $\text{Cl}^*$ $\pm\text{SD}$ [ $\text{Cl}^*_{\text{max}}$ ] $\text{mg m}^{-3}$
2108-NSCI	0.35	73±23	105	7.28±1.22	0.07±0.03	0.13	-	46±20 [89]	0	BDL	BDL
2108-NSCI	0.40	73±35	111	5.93±1.03	0.05±0.03	0.13	-	39±20 [77]	0.004±0.02	BDL	BDL
2108-SCI	0.07	47±40	108	7±1.50	0.05±0.05	0.13	-	21±16 [49]	0±0	0.0024±0.001 [0.004]	0.003±0.0005 [0.004]
2108-SCI	0.08	62±40	111	6.05±1	0.05±0.04	0.10	-	42±28 [80]	0±0	0.06±0.03 [0.09]	0.02±0.02 [0.06]
2108-SCI	0.08	92±35	134	7.54±0.86	0.11±0.06	0.23	-	44±17 [79]	0±0	0.003±0.0004 [0.02]	0.0005±0.0003 [0.001]
2308-NSCI	1.99	65±60	167	10.72±2.86	0.19±0.17	0.48	0.13	30±27 [68]	0±0	BDL	BDL
2308-NSCI	1.48	177±104	360	9.70±2.42	0.42±0.34	1.11	0.41	101±57 [185]	0.01±0.01	BDL	BDL
2308-NSCI	1.33	254±173	541	10.26±1.31	0.69±0.48	1.57	0.61	121±84 [262]	0.01±0.01	BDL	BDL
2308-NSCI	1.16	254±184	528	9.40±3.22	0.80±0.66	2.00	0.88	116±75 [210]	0.31±2.65	BDL	BDL
2308-NSCI	0.80	208±198	538	6.57±2.60	0.32±0.44	1.22	0.80	107±84 [221]	0.05±0.04	0.001±0.0005 [0.001]	BDL
2308-SCI	0.31	402±194	733	6.74±0.84	0.42±0.22	0.69	0.92	144±69 [323]	0±0	0.03±0.02 [0.08]	0.014±0.01 [0.02]
2308-SCI	0.31	236±192	482	5.90±1.64	0.23±0.20	0.54	0.72	90±67 [169]	0±0	0.004±0.003 [0.01]	0.0005±0.0002 [0.0008]
2308-SCI	0.96	186±158	477	7.30±3.01	0.35±0.31	0.97	0.51	81±71 [196]	0.002±0.007	0.005±0.001 [0.008]	0.011±0.003 [0.015]
2308-SCI	1.64	200±139	488	10.41±1.50	0.62±0.51	1.74	0.57	83±53 [198]	0.53±0.50	0.17±0.10 [0.29]	0.12±0.08 [0.21]
2308-SCI	1.60	162±120	332	9.70±3.00	0.50±0.38	1.04	0.34	71±54 [157]	0±0	0.003±0.0001 [0.005]	0.003±0.0001 [0.004]
2308-SCI	1.60	184±139	404	9.50±2.82	0.57±0.58	1.55	0.51	95±63 [183]	0.41±0.43	0.01±0.01 [0.02]	0.023±0.02 [0.08]
2308-SCI	2.26	175±107	320	13.10±1.14	0.80±0.50	1.49	0.38	83±51 [155]	0.43±0.52	0.18±0.12 [0.40]	0.11±0.10 [0.28]
2408-NSCI	0.21	92±92	244	5.55±1.76	0.06±0.06	0.18	0.31	56±59 [147]	0±0	0.0008±0.0003 [0.001]	0.002±0.002 [0.005]
2408-SCI	0.20	159±153	413	5.57±1.76	0.14±0.15	0.41	0.70	65±57 [157]	0±0	0.002±0.0001 [0.003]	0.001±0.001 [0.002]
2408-SCI	0.20	161±189	649	5.91±2.06	0.16±0.18	0.56	0.96	70±88 [321]	0±0	0.01±0.01 [0.02]	0.004±0.003 [0.01]
2408-SCI	0.20	300±171	603	6.58±1.30	0.32±0.19	0.54	0.93	111±72 [347]	0±0	0.02±0.01 [0.05]	0.01±0.01 [0.02]

432 (i) At nearly  $D^* = 0.96$  km, smaller mean concentrations of  $N_t$  ( $186 \pm 158 \text{ cm}^{-3}$ ) are noted for  
433 SCl compared to the NSCl ( $N_t = 208 \pm 198 \text{ cm}^{-3}$ ) cloud pass at  $D^* = 0.80$  km. At these two nearly  
434 similar levels, the mean  $r_e$  values for the SCl case ( $r_e = 7.30 \pm 3.01 \text{ }\mu\text{m}$ ) were greater than those for the  
435 NSCl case ( $r_e = 6.57 \pm 2.60 \text{ }\mu\text{m}$ ). At greater  $D^*$  of 1.60 km ( $r_e = 9.50 \pm 2.82 \text{ }\mu\text{m}$ ) and 2.26 km  
436 ( $r_e = 13.10 \pm 1.14 \text{ }\mu\text{m}$ ), drizzle drops (see Table 3) were noted in the SCl cases. This may indicate  
437 active CC process in the SCl case. The mean DSDs are shown in Fig. 7(d,e) selected considering the  
438 criteria  $0.75 < \text{LWC}/\text{LWC}_{\text{max}} < 1$  of the cloud transects. The corresponding AF values indicated on  
439 the panels suggest active entrainment and mixing processes in these clouds. The production of  
440 drizzle in some of the clouds may also lower the AF values which means that the dilution rate is not  
441 accurate in such clouds. The seeding effect may give rise to the initial production of drizzle particles,  
442 which were seen within the tail of the DSDs. Hence, the tail effect of the seeding particles appears to  
443 be active. Note that since the cloud passes were made in the developing stage of the cloud, these  
444 drizzle drops were formed spontaneously, not falling from the cloud tops because their terminal  
445 velocities are less than the updraft velocities. The broadening of the DSDs will serve to further  
446 increase the efficiency of the CC process (Andreae, et al, 2004; Rosenfeld et al., 2008; Rosenfeld et  
447 al., 1994; Freud et al., 2012; Konwar et al., 2012) leading to the production of drizzle drops at higher  
448  $D^*$ s. Also, stronger updrafts ( $\approx 5 \text{ ms}^{-1}$ ) were observed in SCl (see Fig. S4n), which helped in the  
449 growth of larger-sized droplets.

450 The formation of drizzle drops ( $D > 100 \text{ }\mu\text{m}$ ) in the SCl was noted (Fig. 7(e,f) and Fig. S4) while no  
451 significant drizzle concentrations were noticed for NSCl (Fig. S3). The difference in drizzle  
452 concentration suggests that the flare particles modulate the mid-size cloud droplets ( $D \approx 14 \text{ }\mu\text{m}$ ) that  
453 grow further by diffusion process. As the drizzle drops fall under the influence of gravity, stronger  
454 downdrafts are most likely due to the cooling by evaporation (see Fig. S4n). Moreover, small

455 droplets of  $D \leq 11 \mu\text{m}$  were observed at high altitudes for both clouds (Table 3). The scatter plots  
456 between  $r_e\text{-K}^*$  and  $r_e\text{-Cl}^*$  are shown in Fig. S5. The prevailing dynamical conditions e.g., vertical  
457 velocity are also indicated. It is found that the larger sized droplets (greater  $r_e$  values) are associated  
458 with the larger mass concentrations of  $\text{K}^*$  and  $\text{Cl}^*$ , in the SCl. In both the updrafts and downdrafts,  
459 all these chemical species were present. Having found the seeding tracers  $\text{Cl}^*$  and  $\text{K}^*$  at different  
460 altitudes, it may be emphasized that the modification of cloud properties occurs due to the dispersal  
461 of seeding particles through the cloud base. Seeding particles were present at deeper  $D^*$ s as the  
462 cloud droplets were transported through updrafts and re-circulated as the cloud developed (Khain et  
463 al., 2013).

464 It is important to note that the differences in cloud microphysical properties observed between the  
465 seeded and unseeded clouds could be a result of natural variability, and more data are needed to  
466 arrive at a statistically significant result. However, given that these differences were accompanied  
467 by statistically different concentrations of chemical composition in the cloud droplet residues in the  
468 same environmental conditions, the evidence is compelling that seed material has a) transported to  
469 altitudes above the cloud base where they were released and b) these aerosol particles have  
470 influenced cloud microphysical processes.

471

### 472 **3.2.3 Case iii: 24 August 2019.**

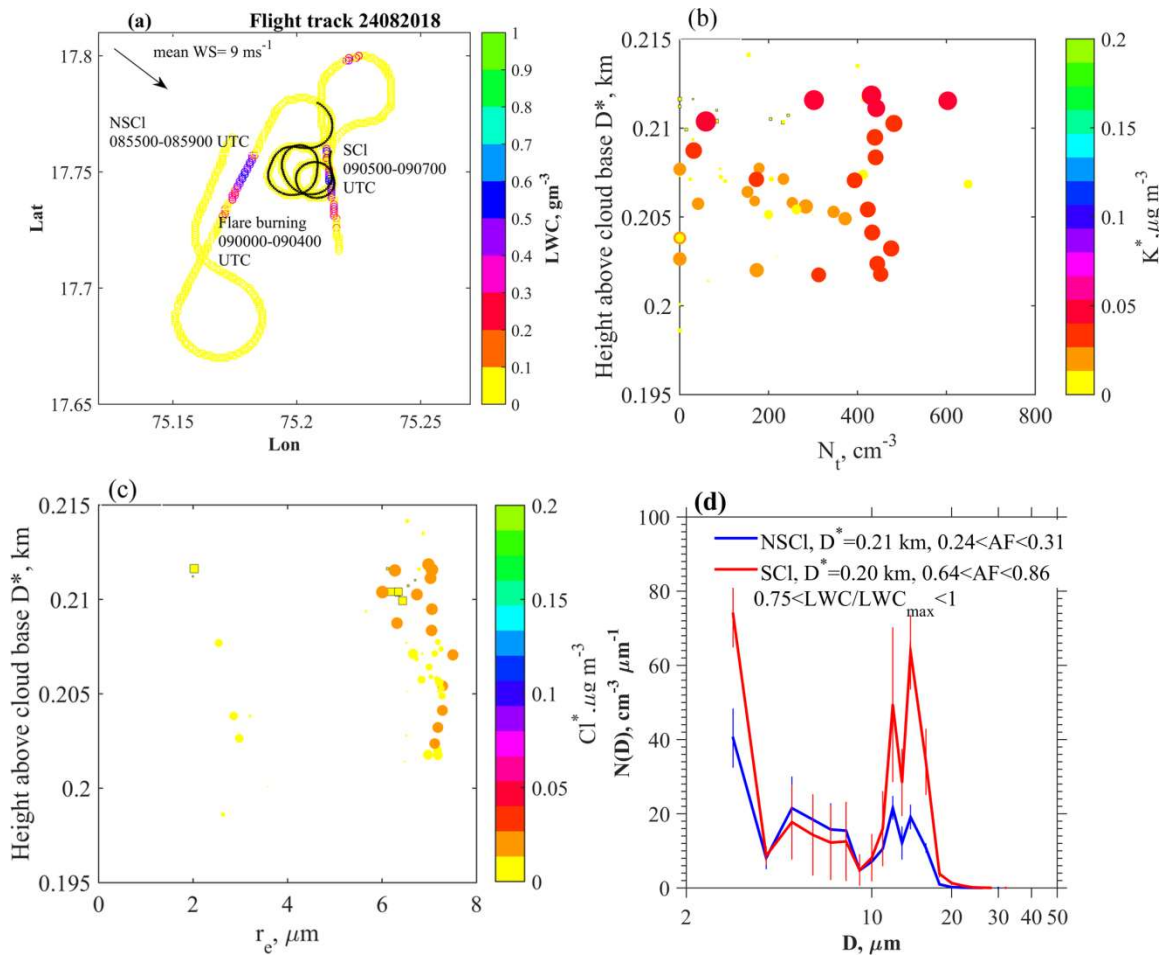
473 The third cloud seeding case was carried out on an isolated convective cloud. The flight path is  
474 shown in Fig. 8a. South-westerly winds with a mean speed of  $9 \text{ m s}^{-1}$  were noted near the cloud base  
475 at 2.1 km with a maximum updraft of  $8 \text{ m s}^{-1}$ . One cloud pass before the flare dispersal was made  
476 from 08:55-08:59 UTC above the cloud base at  $\approx 2.3 \text{ km}$ . Three downwind cloud passes during

477 09:05-09:07 UTC were made at  $\approx 2.3$  km after the flares were burned. The variations of  $N_t$ , and  $r_e$   
478 *w.r.t.*  $D^*$  are shown in Figs. 8b,c. Increased mass concentrations of  $K^*$  and  $Cl^*$  are noted in SCl cases  
479 that identify the seeded clouds. The DSD properties of the clouds are shown in supplementary Fig.  
480 S6 & S7 and their parameters are indicated in Table 3. The mean DSDs (Fig. 8d) indicate increased  
481 droplet concentration in the small and mid-drop diameter ranges. Note that the AF values indicated  
482 strong dilution in the NSCl DSDs, which may also impact the observed differences in the droplet  
483 number densities. No marginal increment in  $r_e$  values was observed in the SCl. Another aspect to  
484 consider here is the effect of strong updraft of  $8 \text{ m s}^{-1}$ . Using the Twomey (1959) equation the  
485 maximum droplet concentration formed in an updraft ( $W$ ) can be expressed in terms of  $W$  and CCN-  
486 SS spectra, i.e.  $N_{CCN} = C SS^k$  i.e. (Roger and Yau, 1989),

$$487 \quad N \approx 0.88 C^{2/(k+2)} [7 \times 10^{-2} W^{3/2}]^{k/(k+2)} \quad (4)$$

488 Here,  $W$  is in  $\text{cm s}^{-1}$ ,  $N_{CCN} = 799 SS^{0.43}$ , which is obtained from the CCN counter (Roberts and  
489 Nenes, 2005; Nenes et al., 2001 and reference therein) operated in the research aircraft. During the  
490 cloud passes, maximum updrafts of  $W = 2.89 \text{ m s}^{-1}$ ,  $1.00 \text{ m s}^{-1}$  and  $1.91 \text{ m s}^{-1}$  were obtained. These  
491 values suggest that droplets formed in these updrafts could be  $593 \text{ cm}^{-3}$ ,  $448 \text{ cm}^{-3}$  and  $531 \text{ cm}^{-3}$ ,  
492 respectively. If we use the maximum updraft speed of  $8 \text{ m s}^{-1}$  measured below cloud base, the droplet  
493 concentrations formed in this updraft could be as high as  $777 \text{ cm}^{-3}$ . In this scenario, the  
494 supersaturation could be greater than 1%, which can activate small-sized CCN. Therefore, the  
495 presence of strong updrafts that yield high SS could be one reason for the increasing  $N_t$  in the seeded  
496 clouds; while dry air mixing in the NSCl cases could be another reason for the smaller concentration  
497 of  $N_t$ . These processes may be attributed for the change in LWC values in the SCl cases.

498



500  
 501 **Figure 8.** (a) Flight path during the seeding experiment on 24 August 2019. Periods during which  
 502 cloud measurements were made for NSCI and SCI are indicated. The black line indicates the flare  
 503 burning. Profiles of (b)  $N_t$ , and (c)  $r_e$ , *w.r.t.*  $D^*$  (km). The parameters are indicated with the mass  
 504 concentrations of  $K^*$ , ( $\mu\text{g m}^{-3}$ ), and  $Cl^*$  ( $\mu\text{g m}^{-3}$ ). (d) Mean DSDs with standard deviations indicated  
 505 by the vertical bars, of clouds ( $0.75 < LWC/LWC_{\text{max}} < 1$ ) above the cloud base, for NSCI and SCI. The  
 506 adiabatic LWC fractions corresponding to the DSDs are also indicated.

507

508

509

510

#### 511 **4. Summary and conclusions:**

512           The successful identification of seeded cloud hydrometeors, and the tracing back to their  
513 seeding origins in cloud seeding experiments has been an outstanding challenge for cloud seeding  
514 operations. The unequivocal identification of seeding material within clouds was the primary  
515 difficulty in such experiments. During the CAIPEEX 2019 seeding experiments conducted in India,  
516 we measured cloud microphysical properties and traced the seeding material with an mAMS behind  
517 a CVI in convective and stratus clouds.

518 In our experiments, the mAMS identified an enhancement of both K and Cl mass concentrations,  
519 most likely from the oxidizing agent (KClO) and seed material (CaCl<sub>2</sub>). In stratus and convective  
520 clouds, such enhanced concentrations of refractory K and Cl should be considered as a seeding  
521 signature.

522 Enhanced small-sized droplet concentrations that were measured near the cloud base of convective  
523 clouds and in a warm stratus layer are noted. This result indicates that during the monsoon season  
524 with an available moisture supply, even the small-sized CCN present in the seed material could be  
525 activated into cloud droplets. The presence of strong updrafts near the cloud base of isolated  
526 convective clouds could also play a major role in the activation of small-sized CCN to cloud  
527 droplets. These strong updrafts would yield high supersaturation values, thus activating small-sized  
528 CCN. The impact of strong updrafts on the activation of cloud droplets, especially when seeding  
529 agents are dispersed below the cloud base, requires more focused attention and study.

530 In the case of a convective cloud, clear differences in the cloud microphysical properties of SCl  
531 compared to NSCl are noted. The flare materials released below the cloud base were lifted to a

532 height of 2.25 km above the cloud base. In the lower part of the SCl larger droplet concentrations  
533 were noted. The SCl also had a larger  $r_e$  than the NSCl at similar heights above the cloud base. The  
534 seeded clouds contained more drizzle drops, suggesting that they reached the threshold for warm  
535 rain initiation at a lower distance from the cloud base than the non-seeded clouds. These results from  
536 the limited sample indicate the plausible tail effect of the largest particles in the flares, initiating  
537 large cloud drops and drizzle. Though this case study indicate the importance tails effect; conclusive  
538 evidence would require much more data.

539 Whether competition or the tail effect is important in a successful cloud experiment remains to be  
540 examined, as the prevailing dynamical conditions can play a significant role in controlling the cloud  
541 microphysical processes. These complexities need to be addressed with more experiments using  
542 mAMS.

543 This study identifies a novel methodology to simultaneously track and measure the cloud seeding  
544 signatures and to assess how the seeding alters the microphysical properties of clouds leading to  
545 raindrop formation. The utilization of an mAMS in cloud seeding experiments together with a CVI  
546 allows for identifying the seeded cloud parcels of interest, leading to a better understanding of the  
547 effects on the microphysical properties of the cloud. Although these measurements of flare material  
548 in seeded clouds are associated with changes in physical properties, the data set is too limited to  
549 unequivocally assert that this methodology will always be successful. Future studies with a much  
550 larger data set will provide more statistical evidence linking seed aerosol and increases in  
551 precipitation.

552 **Acknowledgment:** Indian Institute of Tropical Meteorology, Pune and the CAIPEEX project are  
553 funded by the Ministry of Earth Sciences, Govt. of India. We thank Director, IITM for continuous

554 supports. The authors are grateful to the team members, the ground staff, V. Ruge and S. Patil of  
555 M/S Tesscorn AeroFluid, Inc., and the pilots for their dedicated efforts in conducting the project.  
556 The authors are grateful to the Editor and two anonymous reviewers for their insightful suggestions  
557 that helped improve the manuscript.

#### 558 **Data availability**

559 mAMS and Cloud data are available at:

560 <https://iitmcloud.tropmet.res.in/index.php/apps/files/?dir=/&fileid=59847#>

561

#### 562 **Author contributions**

563 TP and DW designed the mAMS experiment; MK, BW and ECF prepared the initial draft; KH,  
564 MK, BW, ECF, SC, SB, NM, MV, SJ and TP participated in the aircraft experiment; DB, TP, DW,  
565 DA, PM, MK, BW, ECF, MV, SC, SB and SAD reviewed the manuscript. All authors agree with the  
566 final version of the manuscript.

#### 567 **Competing interests**

568 The contact author has declared that none of the authors has any competing interests.

#### 569 **References:**

570 Anderson, B. E., Cofer, W. R., Bagwell, D. R., Barrick, J. W., & Hudgins, C. H.. Airborne  
571 observations of aircraft aerosol emissions I: Total nonvolatile particle emission indices. *Geophysical*  
572 *Research Letters*, 25, 1689–1692, 1998.

573 Andreae, M. O., Rosenfeld, D., Artaxo, P., Costa, A. A., Frank, G. P., Longo, K. M., and Silva-  
574 Dias, M. A. F.: Smoking rain clouds over the Amazon, *Science*, 303, 1337–1342, 2004.

575 Baumgardner, D.: An analysis and comparison of five water droplet measuring instruments. *J. Appl.*  
576 *Meteor.*, 22, 891-910, 1983.

577 Baumgardner, D., H. Jonsson, W. Dawson, D. O'Connor and R. Newton. : The cloud, aerosol and  
578 precipitation spectrometer (CAPS): A new instrument for cloud investigations, *Atmos. Res.*, 59-60,  
579 251-264, 2001.

580 Baumgardner, D., S. Abel, D. Axisa, R. Cotton, J. Crosier, P. Field, C. Gurganus, A. Heymsfield, A.  
581 Korolev, M. Krämer, P. Lawson, G. McFarquhar, J. Z Ulanowski, J. Shik Um,: Chapter 9: Cloud Ice  
582 Properties - In Situ Measurement Challenges, AMS Monograph on Ice Formation and Evolution in



583 Clouds and Precipitation: Measurement and Modeling Challenges, Eds. D. Baumgardner, G.  
584 McFarquhar, A. Heymsfield, Boston, MA., 2016.

585 Bowen, E. G.: A new method of stimulating convective clouds to produce rain and hail, Quarterly  
586 Journal of Royal Meteorological Society, 78, 37–45, 1952.

587 Bruintjes, R. T.: A review of cloud seeding experiments to enhance precipitation and some new  
588 prospects, Bulletin of the American Meteorological Society, 80, 805-820, 1999.

589 Bruintjes, R. T., Clark, T. L., and Hall, W. D.: The dispersion of tracer plumes in mountainous  
590 regions in central Arizona: Comparisons between observations and modeling results, Journal of  
591 Applied Meteorology, 34, 971-988, 1995.

592 Bruintjes, R. T., Salazar, V., Semeniuk, T. A., Buseck, P., Breed, D. W., and Gunkelman, J.:  
593 Evaluation of Hygroscopic Cloud Seeding Flares, The Journal of Weather Modification, 44(1), 69–  
594 94. <https://doi.org/10.54782/jwm.v44i1.85>, 2012.

595 Canagaratna, M. R., Jayne, J.T., Jimenez, J.L., Allan, J.D., Alfarra, M.R., Zhang, Q.,  
596 Onasch, T.B., Drewnick, F., Coe, H., Middlebrook, A., Delia, A., Williams, L.R., Trimborn, A.M.,  
597 Northway, M.J., DeCarlo, P.F., Kolb, C.E., Davidovits, P. and Worsnop, D.R.: Chemical and  
598 microphysical characterization of ambient aerosols with the aerodyne aerosol mass spectrometer.  
599 Mass Spectrometer Reviews, 26, 185–222, 2007.

600 Cooper, W. A., Bruintjes, R. T. and Mather, G. K.: Calculations pertaining to hygroscopic seeding  
601 with flares, Journal of Applied Meteorology, 36, 1449-1469, 1997.

602 DeCarlo, P. F., Kimmel, J. R., Trimborn, A., Northway, M. J., Jayne, J. T., Aiken, A. C., Gonin,  
603 M., Fuhrer, K., Horvath, T., Docherty, K.S., Worsnop, D. R. and Jimenez, J. L.: Field-deployable,  
604 high-resolution, time-of-flight aerosol mass spectrometer. Analytical Chemistry, 78, 8281–8289,  
605 2006.

606 Drewnick, F., Diesch, J. M., Faber, P., and Borrmann, S.: Aerosol mass spectrometry: particle–  
607 vaporizer interactions and their consequences for the measurements, *Atmospheric Measurement and*  
608 *Techn.*, 8, 3811-3830, 2015.

609 Flossmann, A., Michael, M., Abshaev, A., Bruintjes R., Masataka, M., Prabhakaran T. and Zhanyu,  
610 Y.: Review of advances in precipitation enhancement research, Bulletin of the American  
611 Meteorological Society, 100, 1465–1480, 2019.

612 Freud, E. and Rosenfeld, D.: Linear relation between convective cloud drop number concentration  
613 and depth for rain initiation, J. Geophys. Res. Atmosphere, 117, D02207, 2012.

614 French, J. R., Friedrich, K., Tessorf, S. A., Rauber, R. M., Geerts, B., Rasmussen, R. M., Xue,  
615 L., Kunkel, M. L. and Blestrud, D. R.: Precipitation formation from orographic cloud seeding.  
616 Proceeding of National Academy of Sciences, United States of America, 115, 1168–1173, 2018.

617 Friedrich, K., Ikeda, K., Tessendorf, S. A., French, J. R., Rauber, R. M., Geerts, B., Xue, L.,  
618 Rasmussen, R. M., Blestrud, D. R., Kunkel, M. L., Dawson, N. and Parkinson, S: Quantifying  
619 snowfall from orographic cloud seeding, *Proc. Natl. Acad. Sci. U. S. A.*, 117(10): 5190–5195, 2020,  
620 doi: 10.1073/pnas.1917204117.

621 Gayatri, K., Prabhakaran T., Malap N., Konwar M., Gurnule D., Bankar S. and Murugavel P.:  
622 Physical evaluation of hygroscopic cloud seeding in convective clouds using in situ observations and  
623 numerical simulations during CAIPEEX, *Atmos. Res.*, 284: 106558, 1-17, 2023,  
624 DOI:10.1016/j.atmosres.2022.106558.

625 Ghate, V. P., Albrecht, B. A., Kollias, P., Jonsson, H. H. and Breed, D. W.: Cloud seeding as a  
626 technique for studying aerosol-cloud interactions in marine stratocumulus, *Geophysical Research*  
627 *Letters*, 34, L14807, 2007.

628 Giordano, M. R., Kalnajs, L. E., Goetz, J. D., Avery, A. M., Katz, E., May, N. W., Leemon, A.,  
629 Mattson, C., Pratt, K. A., and DeCarlo, P. F.: The importance of blowing snow to halogen-  
630 containing aerosol in coastal Antarctica: influence of source region versus wind speed, *Atmos.*  
631 *Chem. Phys.*, 18, 16689–16711, <https://doi.org/10.5194/acp-18-16689-2018>, 2018.

632 Golderger, L. A., Pekour, M. S., and Hubbe, J. M.: Counterflow Virtual Impactor (CVI) Inlet  
633 Aboard Aircraft (INLETCVI-AIR) Instrument Handbook, DOE/SC-ARM-TR-254,  
634 [https://www.arm.gov/publications/tech\\_reports/handbooks/doe-sc-arm-tr-254.pdf](https://www.arm.gov/publications/tech_reports/handbooks/doe-sc-arm-tr-254.pdf), 2020.

635 Hindman, E. E.: Water droplet fogs formed from pyrotechnically generated condensation nuclei, *J.*  
636 *of Weather. Modif.*, 10, 77-96, 1978.

637 Jayne, J. T., Leard, D. C., Zhang, X., Davidovits, P., Smith, K. A., Kolb C. E., and Worsnop, D. R.:  
638 Development of an Aerosol Mass Spectrometer for Size and Composition Analysis of Submicron  
639 Particles, *Aerosol Science and Technology*, 33:1-2, 49-70, DOI: [10.1080/027868200410840](https://doi.org/10.1080/027868200410840), 2000.

640 Khain, A. P, Prabha, T. V., Benmoshe, N., Pandithurai, G. and Ovchinnikov, M.: The mechanism  
641 of first raindrops formation in deep convective clouds, *J. Geophys. Res.*, 118, 9123-9140, 2013.

642 Konwar, M., Maheskumar, R. S., Kulkarni, J. R., Freud, E., Goswami, B. N. and Rosenfeld, D.:  
643 Aerosol control on depth of warm rain in convective clouds, *J. Geophys. Res.*, 117, D13204, 2012.  
644 doi:10.1029/2012JD017585.

645 Konwar, M., Prabhakaran, T., Khain, A. and Pinsky, M.: Cloud microphysical structure analysis  
646 based on high-resolution in-situ measurements, *J. Atmospheric Sci.*, 78, 2265-2285, 2021.

647 Konwar, M., Malap, N., Hazra, A., Axisa, D., Prabhakaran, T., and Khain, A.: Measurement of  
648 Flare Size Distribution and Simulation of Seeding Effect with a Spectral Bin Parcel Model, *Pure and*  
649 *Applied Geophysics*, 180, 3019–3034, 2023, <https://doi.org/10.1007/s00024-023-03293-z>.

650

651 Korolev, A. V., Isaac, G. A., Strapp, J. W., Cober, S. G., and Barker, H. W. : In situ measurements  
652 of liquid water content profiles in midlatitude stratiform clouds , Q. J. R. Meteorol. Soc. 133: 1693–  
653 1699, 2007, DOI: 10.1002/qj.147.

654  
655

656 Kuba, N., and Murakami, M.: Effect of hygroscopic seeding on warm rain clouds—numerical study  
657 using a hybrid cloud microphysical model, Atmos. Chem. Phys., 2010, 10, 3335–3351.

658

659 Kulkarni, J. R., Maheshkumar, R. S., Morwal, S. B., Padma Kumari B., Konwar M., Deshpande  
660 C.G., Joshi R. R., Bhalwankar R.V., Pandithurai G., Safai P.D., Narkhedkar S.G, Dani K. K., Nath  
661 A., Nair, S., Sapre, V.V, Puranik P.V., Kandalgaonkar S., Mujumdar V. R., Khaladkar R.M.,  
662 Vijayakumar R., Thara P. and B. N.Goswami: The cloud aerosol interaction and precipitation  
663 enhancement experiment (CAIPEEX): Overview and preliminary results. Current Science, 12, 413-  
664 425, 2012.

665

666 Lance, Sara, C. A. Brock, Dave Rogers, and J. A. Gordon.: Water droplet calibration of the Cloud  
667 Droplet Probe (CDP) and in-flight performance in liquid, ice and mixed-phase clouds during  
668 ARCPAC, Atmospheric Measurement Techniques 3, no. 6, 1683-1706, 2010.

669

670 Manton, M., Stone, R. C., Pepler, A., Collins, D. R., Bringi, V. N., Thurai, M., Turner, L. and  
671 McRae, D.: The Queensland Cloud Seeding Research Program, Bulletin of the American  
672 Meteorological Society, <https://doi.org/10.1175/BAMS-D-11-00060.1>, 75–90, 2012.

673

674 Martin, G. M., Johnson, D. W. and Spice, A.: The measurement and parameterisation of effective  
675 radius of droplets in warm stratocumulus clouds, J. Atmos. Sci., 51, 1823-1842, 1994.

676

677 Mather, G. K., Dixon, M. J. and de Jager, J. M.: Assessing the potential for rain augmentation—the  
678 Nelspruit randomized convective cloud seeding experiment, Journal of Applied Meteorology, 35,  
679 1465-1482, 1996.

680

681 Mather, G. K., Terblanche, D. E., Steffens, F. E. and Fletcher, L.: Results of the South African cloud  
682 seeding experiments using hygroscopic flares, Journal of Applied Meteorology, 36, 1433-1447,  
683 1997.

684

685 Nenes , A. , Chuang , P. , Flagan , R. C. and Seinfeld , J. H.: A Theoretical Analysis of Cloud  
686 Condensation Nucleus (CCN) Instruments . J. Geophys. Res , 106 , 3449 – 3474, 2001.

687

688 Noone, K. J., Ogren, J. A., Heintzenberg, J., Charlson, R. J., and Covert D. S.: Design and  
689 calibration of a counterflow virtual impactor for sampling of atmospheric fog and cloud droplets,  
690 Aerosol Science and Technology 8(3): 235–244, <https://doi.org/10.1080/02786828808959186>, 1988.

688 Ogren, J. A., Heintzenberg, J., and Charlson, R. J.: In-situ sampling of clouds with a droplet to  
689 aerosol converter. *Geophys. Res. Lett.*, 121–124,12, 1985.

690 Ogren, J. A., Heintzenberg, J., and Charlson, R. J.: Virtual impactor. US Patent No. 4, 689,052,  
691 1987.

692 Patade, S., Kulkarni, G., Patade, S., Deshmukh, A., Dangat, P., Axisa, D., Prabha, T. V.: Role of  
693 liquid phase in the development of ice phase in monsoon clouds: Aircraft observations and  
694 numerical simulations. *Atmos. Res.*, 229, 157–174, 2019.  
695 <https://doi.org/10.1016/j.atmosres.2019.06.022>

696 Patade, S., Prabha, T. V., Axisa, D., Gayatri, K., Heymsfield, A.: Particle size distribution properties  
697 in mixed-phase monsoon clouds from in situ measurements during CAIPEEX *Jour. of Geophys. Res.*  
698 *Atmos.*, 120, 19, 2015.

699 Prabha, T. V., Khain, A., Maheshkumar, R. S., Pandithurai, G., Kulkarni, J. R., Konwar, M, and  
700 Goswami, B. N.: Microphysics of premonsoon and monsoon clouds as seen from *in situ*  
701 measurements during the Cloud Aerosol Interaction and Precipitation Enhancement Experiment  
702 (CAIPEEX), *J. Atmos. Sci.*,68, 1882–1901, 2011.  
703

704 Prabhakaran, T., Murugavel, P., Konwar M., Malap, N., Gayatri, K., Dixit, S., Samanta, S.,  
705 Chowdhuri., S., Bera, S., Varghese, M., Rao, J., Sandeep, J., Safai, P. D., Sahai, A. K., Axisa, D.,  
706 Karipot, A., Baumgardner, D., Werden, B., Fortner, Ed, Hibert, K., Nair, S., Bankar, S., Gurnule, D.,  
707 Todekar, K., Jose, J., Jayachandran, V., Soyam, P. S., Gupta, A., Choudhary, H., Aravindhavel, A.,  
708 Kantipudi, S. B., Pradeepkumar, P., Krishnan, R., Nandakumar, K., DeCarlo, P. F., Worsnop, D.,  
709 Bhat, G. S., Rajeevan, M., and Nanjundiah, R.: CAIPEEX - Indian cloud seeding scientific  
710 experiment , *Bulletin of American Meteorological Society*, 2023, [https://doi.org/10.1175/BAMS-D-](https://doi.org/10.1175/BAMS-D-21-0291.1)  
711 [21-0291.1](https://doi.org/10.1175/BAMS-D-21-0291.1)

712

713 Roberts , G. C. and Nenes , A.: A Continuous-Flow Streamwise Thermal-Gradient CCN Chamber  
714 for Atmospheric Measurements, *Aeros. Sci. Tech.* , 39, 206 – 221, 2005 .

715 Yau, M.K. and Rogers, R.R.: *Short Course in Cloud Physics*. 3rd Edition, Butterworth-Heinemann,  
716 302 p, 1989.

717 Rosenfeld, D., Axisa, D., Woodley, W. and Lahav, R.: A quest for effective hygroscopic cloud  
718 seeding, *Journal of Applied Meteorology and Climatology*, 49, 1548-1562, 2010.

719 Rosenfeld, D., Woodley, W. L., Axisa, D., Freud, E., Hudson, J. G., and Givati, A.: Aircraft  
720 measurements of the impacts of pollution aerosols on clouds and precipitation over the Sierra  
721 Nevada, *J. Geophys. Res.*,113, D15203,doi:10.1029/2007JD009544, 2008.

722 Rosenfeld, D., and Gutman, G.: Retrieving microphysical properties near the tops of potential rain  
723 clouds by multispectral analysis of AVHRR data, *Atmospheric Res.*, 34, 259–283, 1994.

724 Ryan, B. F. and King, W. D.: A critical review of the Australian experience in cloud seeding,  
725 *Bulletin of the American Meteorological Society*, 78, 239-254, 1997.  
726

727 Salcedo, D., Onasch, T. B., Dzepina, K., Canagaratna, M. R., Zhang, Q., Huffman, J. A., DeCarlo, P.  
728 F., Jayne, J. T., Mortimer, P., Worsnop, D. R., Kolb, C. E., Johnson, K. S., Zuberi, B., Marr, L. C.,  
729 Volkamer, R., Molina, L. T., Molina, M. J., Cardenas, B., Bernabé, R. M., Márquez, C., Gaffney, J.  
730 S., Marley, N. A., Laskin, A., Shutthanandan, V., Xie, Y., Brune, W., Leshner, R., Shirley, T., and  
731 Jimenez, J. L.: Characterization of ambient aerosols in Mexico City during the MCMA-2003  
732 campaign with Aerosol Mass Spectrometry: results from the CENICA Supersite, *Atmos. Chem.*  
733 *Phys.*, 6, 925–946, <https://doi.org/10.5194/acp-6-925-2006>, 2006.

734 Segal, Y., Khain, A., Pinsky, M. and Rosenfeld, D.: Effects of hygroscopic seeding on raindrop  
735 formation as seen from simulations using a 2000-bin spectral cloud parcel model, *Atmospheric*  
736 *Research*, 71, 3-34, 2004.

737 Segal, Y., and Pinsky, M. and Khain, A.: The role of competition in raindrop formation.  
738 *Atmospheric Research*, 83, 106-118, 2007.

739 Shingler, T., Dey, S., Sorooshian, A., Brechtel, F. J., Wang, Z., Metcalf, A., Coggon, M.,  
740 Mülmenstädt, J., Russell, L. M., Jonsson, H. H., and Seinfeld, J. H.: Characterisation and airborne  
741 deployment of a new counterflow virtual impactor inlet, *Atmos. Meas. Tech.*, 5, 1259–1269,  
742 <https://doi.org/10.5194/amt-5-1259-2012>, 2012.

743 Silverman, B. A.: A critical assessment of hygroscopic seeding of convective clouds for rainfall  
744 enhancement, *Bulletin of the American Meteorological Society*, 84, 1219-1230, 2003.

745

746 Stith, J. L., Griffith, D. A., Lynn Rose, R., Flueck, J. A., Miller, Jr. J. R., and Smith, P. L.:  
747 Aircraft observations of transport and diffusion in cumulus clouds, *Journal of Applied Meteorology*  
748 *and Climatology*, 25, 1959-1970, 1986.

749

750 Stith, J. L., Detwiler, A. G., Reinking, R. F. and Smith, P. L.: Investigating transport, mixing, and  
751 the formation of ice in cumuli with gaseous tracer techniques, *Atmospheric Research*, 25, 195-216,  
752 1990.

753 Tessendorf, S. A.; Brientjes, R. T., Weeks, C., Wilson, J. W., Knight, C. A., Roberts, R. D., Peter, J.  
754 R., Collis, S., Buseck, P. R., Freney, E., Dixon, M., Pocerlich, M., Ikeda, K., Axisa, D., Nelson,  
755 E., May, P. T., Richter, H., Piketh, S., Burger, R. P., Wilson, L., Siems, S. T., Manton, M., Stone,  
756 R. C., Pepler, A., Collins, D. R., Bringi, V. N., Thurai, M., Turner, L. and McRae, D.: The

757 Queensland Cloud Seeding Research Program. Bull. Amer. Meteor. Soc., Vol. 89, pp75–90, 2012,  
758 <https://doi.org/10.1175/BAMS-D-11-00060.1>

759 Wang, B. and Laskin, A.: Reactions between water-soluble organic acids and nitrates in  
760 atmospheric aerosols: Recycling of nitric acid and formation of organic salts. J. Geophys. Res., 119,  
761 3335-3351, 2014.

762 WMO: Report on the WMO international workshop on hygroscopic seeding: Experimental results,  
763 physical processes, and research needs, WMP Rep 35, WMO/TD Rep 1006 36, 68pp, 2000.

764 Xue, L., Weeks, C., Chen, S., Tessendorf, S. A., Rasmussen, R. M., Ikeda, K., Kosovic, B.,  
765 Behringer, D., French, J. R., Friedrich, K., Zaremba, T. J., Rauber, R. M., Lackner, C. P., Geerts, B.,  
766 Blestrud, D., Kunkel, M., Dawson, N. and Parkinson, S.: Comparison between Observed and  
767 Simulated AgI Seeding Impacts in a Well-Observed Case from the SNOWIE Field Program  
768 Journal of Applied Meteorology and Climatology, page 345–367, 2022. <https://doi.org/10.1175/JAMC->  
769 [D-21-0103.1](https://doi.org/10.1175/JAMC-D-21-0103.1)

770